RSC Advances

ROYAL SOCIETY OF CHEMISTRY

www.rsc.org/advances

Polyol synthesis of non-stoichiometric Mn-Zn ferrite nanocrystals: structural microstructural characterization and catalytic application.

Z. Beji,[1,2] M. Sun,[3] L. S. Smiri,[2] F. Herbst,[1] C. Mangeney,[1] S. Ammar[1,]*

[1] ITODYS, Université Paris Diderot, Sorbonne Paris Cité, CNRS UMR-7086, Paris 75251, France.

[2] LSSMI, Faculté des Sciences de Bizerte, UR 99/12-30, Zarzouna 7021, Tunisia

[3] School of Chemical Engineering and Light Industry, Guangdong University of Technology, Guangzhou 510006, People's Republic of China

(*) Email: ammarmer@univ-paris-diderot.fr

Address: 15 rue Jean-Antoine de Baïf 75205 Paris cedex 13 France

Phone: (33)1 44 27 86 09 / Fax: (33)1 44 27 61 37

ABSTRACT.

The structure of polyol-made Mn-Zn ferrite powders was investigated by X-ray diffraction, X-ray Photoelectron spectrometry and X-ray absorption spectroscopy. It was found to be a defect-spinel structure in relation with a non-stoichiometry introduced by the mixed oxidation-state of Mn and Fe cations. The ionic defects were identified as cation vacancies mainly located in the octahedral sites. The microstructure of these ferrites was studied by X-ray-diffraction and transmission electron microscopy. They appear to be constituted by quasi-isotropic monodisperse nano-aggregates which consist of pseudo-single crystals. Considering their reduced size, high crystalline quality, and cation mixed valence state related to their non-stoichiometry, the produced particles appear to be particularly valuable for redox-based solid-gas catalytic reactions. They exhibit an interesting activity toward catalytic combustion of dimethyl ether.

KEYWORDS.

Ferrite spinels, Nanoparticles, Polyol process, HRTEM, XPS, EXAFS, Catalytic combustion of dimethyl ether.

INTRODUCTION

Spinel ferrites with the formula of MFe_2O_4, where M represents a divalent metal (such as Cu, Mn, Mg, Zn or a mixture of them) have attracted extensive attention due to their versatile electromagnetic properties. They have been extensively used for electronic and/or magnetic devices, such as microwave filters, power supplies, radio-frequency coils, transformer cores, permanent magnets among others [1]. When their size is reduced to the nanometer scale, the electromagnetic properties of these ferrites may be very useful for other applications. For instance, they have been considered for biomedicine applications, such as contrast agents for magnetic resonance imaging, drug carriers for magnetically guided delivery or heating sources for hyperthermia cancer therapy [2]. They have been also considered for various organic catalysis reactions since they exhibit improved reactivity under mild reaction conditions and can be easily recovered from reaction systems and reused up to several runs almost without loss of catalytic activity [3]. Spinel ferrite nanoparticles (NPs) are thus typically valuable for catalytic decomposition of gaseous pollutants [4], water gas shift reaction [5] and hydrogen production from oxygenated hydrocarbons [6]. To the best of our knowledge, all these reactions are mainly driven by the chemical composition of the ferrite nanocatalysts (the nature and the valence state of the M cation and its consequence on the ferrite phase stoichiometry), their local structure (cation distribution toward the octahedral and tetrahedral spinel sub-lattices) and their microstructure (size, shape, single or polycrystal character…). Indeed, if the effect of the two latter parameters were intensively studied and more or less understood, a few observations were made on their stoichiometry. Interesting results were obtained on ferrite NPs containing mixed divalent or trivalent cations. For instance, the electro-catalytic activity of nickel ferrite NPs for hydrogen evolution reaction was found to increase in the order of Fe_3O_4 < $(Ni_{0.8}Fe_{0.2})Fe_2O_4$ < $(Ni_{0.4}Fe_{0.6})Fe_2O_4$ [7]. It was also elucidated that the oxidation-reduction potential of methyl blue in aqueous solution, in the presence of cobalt-zinc ferrite NPs at pH = 7 under natural sunlight irradiation, was negative and increased with the increase of the Zn content, leading to a decrease of the methyl blue degradation rate with the increase of the Zn content [8]. Also, the partial replacement of Fe^{3+} ions by the Mn^{3+} ions in Co-Zn ferrite NPs possessing cubic spinel structure $(Co_{0.6}Zn_{0.4})(Fe_{2-x}Mn_x)O_4$, $0<x\leq1$), resulted that the degradation of methyl orange dye was enhanced with an increase in Mn^{3+} ions concentration [9]. These changes are due to the octahedral site preference and higher redox potential of manganese ion as compared to that of iron. Besides, the stoichiometry deviation in these mixed ferrite NPs deviation plays an important role in all these catalytic reactions. Indeed, by comparing the catalytic activity of stoichiometric $(Ni_xZn_{1-x})Fe_2O_4$ NPs and their related oxygen-deficient solid solutions, $(Ni_xZn_{1-x})Fe_2O_{4-\delta}$, toward CO_2 decomposition, the latter showed better efficiencies [10]. This enhancement is mainly attributed to the mixed valence state of iron cations (Fe^{2+}/Fe^{3+}) in the latest ferrites and their role in the electron exchange between adsorbed CO_2 and the nanocatalyst surface. High catalytic performance was also observed on alkali (K^+) doped $CuFe_2O_4$ nanoparticles toward NO_x reduction into N_2, compared to non-doped ones [4]. Doping promoted mixed valence state of copper and/or iron cations at the surface of the catalysts with their potassium enrichment, improving the electron exchange process with the adsorbed NO_x [4].

To take advantageous from these mixed-valence-state cations spinel ferrite NPs for such peculiar applications, it becomes crucial to perfectly tailor their chemical composition and their local structure in term of cation distribution, while maintaining their size in the nanometer scale and avoiding their aggregation and/or coalescence. To achieve this control, a lot of works were devoted to the fabrication of nanoscaled ferrites, focusing of course on cheap and economical processes. Two experimental approaches were nowadays adopted to produce such nanopowders. The first one, and may be the most explored one, consists of a post-synthetic "soft" oxidation or reduction thermal treatment to create defects in particles produced by conventional granular techniques such as co-precipitation, hydrothermal route or ball-milling [10,11,12]. The second one, and very poorly explored one, consists of a voluntary direct fabrication of non-stoichiometric nanoscaled ferrites using wet chemical routes. This may be achieved by introducing in the reaction medium a doping monovalent (Na^+, K^+…) or tetravalent cations (Te^{4+}…) with respect to its solubility limit into the spinel lattice [4] or by balancing between a partial oxidation or reduction of metal cation dissolved in the reactional medium during ferrite synthesis. Such a control may be easily achieved by the polyol process. Indeed, polyols are efficient crystal-growth medium in which reductive and oxidative reactions may take place at moderate temperature (up to the boiling point of the solvent) [13]. Acting on the polyol nature, α-diols or etherglycols, the former being better reducing agents than the latter, the amount of added water [13] and the reaction atmosphere, inert or oxidative [14], it is possible to prepare metal or oxide NPs as it is possible to tune the oxidation state of the metal cations into the latter phases [15].

In this context, we decided to produce non-stoichiometric Mn-Zn ferrite NPs using the polyol process, to check their chemical composition, cation distribution toward the spinel lattice and their morphology as a preliminary study before the evaluation of their redox-based reactivity toward catalytic combustion of dimethyl ether (DME). The characterizations were carried out by combining several techniques, mainly X-ray diffraction (XRD), inductive coupling plasma-atomic emission spectroscopy (ICP) analysis, X-ray photoelectron spectrometry (XPS), X-ray absorption spectroscopy (XAS) and low and high resolution transmission electron microscopy (TEM).

Temperature programmed reduction of hydrogen (H_2-TPR) and temperature programmed desorption of oxygen (O_2-TPD) were also performed on the produced powders before to test them as catalysts for DME combustion.

EXPERIMENTAL SECTION

Chemicals. $Mn(CH_3COO)_2.4H_2O$, $Zn(CH_3COO)_2.2H_2O$, $FeCl_3$ and $NaCH_3CO_2.nH_2O$ (n = 0, 3) and ethyleneglycol (EG) were purchased from SIGMA-ALDRICH and ACROS ORGANICS, respectively, and used without further purification.

Synthesis. The Mn-Zn ferrite particles were prepared by forced hydrolysis in a polyol solvent. In practice, hydrolysis and condensation reactions were carried out on dissolved metallic cations in a polyol solvent. Hydrolysis reaction in favored in basic conditions. So an excess of sodium acetate (Na+ cations are inert) was introduced to basify the reaction medium. So, iron, zinc and manganese acetates were dissolved in 250 mL of EG solvent within the desired nominal molar ratio. Typically, the nominal iron concentration was fixed to 0.2 M and the nominal molar ratio of divalent cations to ferric ions, namely [Zn+Mn]/[Fe], was fixed to 0.6. Required amounts of distilled water amount and sodium acetate base were added (the nominal water and acetate to total metal molar ratio h = $H_2O/(Zn+Mn+Fe)$ and A = Acetate/Zn+Mn+Fe were fixed to 9 and 3, respectively). The mixture is then heated (6 °C/min) under reflux for twelve hours while mechanically stirred. The boiling temperature reached 160-170°C. After cooling to room temperature, the solids were separated from the supernatant by centrifugation, washed three time with a large volume of ethanol to remove organic residue from the surface of the produced particles (mainly adsorbed polyol molecules). This washing protocol is well-established and routinely used. The recovered powders were then dried in air at 50 °C overnight. Two samples were prepared, as representative of the $Zn_{1-x}Mn_xFe_{2.4}O_4$ solid solution, namely a manganese poor and a rich one, corresponding to x = 0.2 and 0.8, respectively. Hereafter, the samples are denoted as P2M and P8M, respectively.

Structural characterization. XRD patterns of the crystalline phases were recorded on a Brucker D8 Advance diffractometer, using Cu Kα radiation, in the 2θ range 10-70°, with steps of 0.02° (2θ) and a step time of 10 s. the cell parameter and the size of coherent diffraction domain (crystal size) were determined with the MAUD software, which is based on the Rietveld method combined with Fourier analysis [16]. Polycrystalline strain-free silicon was used as standard to quantify the instrumental broadening contribution. ICP analysis of Mn, Zn and Fe was performed at the *Service Central d'Analyse* of CNRS at the French facility (Vernaison). The produced powders were prepared by acid digestion using concentrated ultra-high grade HNO_3 solution (69%). XPS measurements were performed using a Thermo VG ESCALAB 250 instrument equipped with a monochromatic Al Kα (hν = 1486.6 eV) 200 W X-ray source. The X-ray spot size was 650 μm. The pass energy was set at 150 and 40 eV for the survey and the narrow scans, respectively. Measurements were carried out on powdered samples mounted on sample holders. Data acquisition and processing were performed with the Avantage software, version 1.85. Extended X-ray Absorption Fine Structure (EXAFS) data were collected for the Mn, Zn and Fe K-edges of the particles at 77 K, using a transmission mode detection scheme with a Si (111) two-crystal monochromator on the XAFS beamline of the ELLETRA storage ring at the Italian facility (Trieste). Data were also similarly collected on commercial powdered samples $ZnFe_2O_4$ (ALFA, 99,9%) and Fe_3O_4 (PROLABO, 99,9%) as standards for Zn and Fe, and MnO (MERCK, >99%), Mn_2O_3 (PROLABO, >99%) and MnO_2 (SIGMA-LADRICH, >99%) as standards for Mn. The samples were ground and homogeneously dispersed in cellulose pellets. EXAFS data were analyzed using the IFEFFIT software [17] with calculated amplitude and phase shift functions from FEFF7 program [18].

Microstructural analysis. Particle morphology was determined by TEM observations using a JEOL-100 CX II microscope operating at 100 kV. The particle size distribution was obtained from the recorded micrographs by using SAISAM software (Microvision Instruments) calculating the surface-average particle diameter of about 400 particles:

Redox and catalytic activity evaluation. H_2-TPR and O_2-TPD plots were measured in a MICROMERITICS AutoChem2920 equipment. To clean their surface, the samples (20-30 mg) were first pretreated in an argon stream (50 mL/min) up to 350 °C during 20 min, for TPR measurements, and in a helium stream (50 mL/min) at 200 °C during 25 min, for TPD ones. After cooling to room temperature, a mixture of 5 vol% H_2 in Ar was admitted onto the samples and temperature was raised up to 750 °C (10 °C /min) for TPR experiments. For TPD experiment, the sample was exposed to O_2 atmosphere for 20 min, and then a helium stream (50 ml/min) was introduced into the system and temperature was raised at a constant rate of 10 ^{o}C /min up to750 ^{o}C. The amount of consumed hydrogen and desorbed oxygen in the effluent gas were detected by a TCD. The catalytic oxidation test was carried out in a fixed-bed continuous flow quartz reactor (8 mm i.d.) at atmospheric pressure. The reactor was charged with 300 mg of catalyst which had been pressed, crushed and sieved to 40~60 meshes. Two reactant gases, DME and 20 vol.% O_2/He, were co-fed into the reactor with a flow of 1 mL/min and 50 mL/min, respectively. The gas hourly space velocity was 10.2 $L.g^{-1}{}_{cat}.h^{-1}$. T_{10} and T_{90} were used for description of the activity, which is the temperature acquired for 10% and 90% DME conversion, respectively. The reactor effluents were analyzed by an online gas chromatography (Agilent 6820) using a methyl silicone capillary column (ATSE30) and a Porapak Q packed column connected to a flame ionization detector and a thermal conductivity detector, respectively. All the connected lines between the reactor and gas chromatograph were kept above 120 °C to prevent condensation.

RESULTS

Evidence of the non-stoichiometry of the produced powders. The chemical analysis shows that oxygen, manganese, zinc and iron atoms are present in both samples. The inferred compositions from ICP measurements are not found in accordance with the expected manganese zinc ferrite stoichiometry. A large manganese and zinc atoms deficiency are evidenced partly compensated by iron atoms excess (Table 1).

	Zn (*wt*.-%)		Mn (*wt*.-%)		Fe (*wt*.-%)	
Sample	*Expected*	*Measured*	*Expected*	*Measured*	*Expected*	*Measured*
P2M	21.9	12.5	4.6	1.9	46.7	49.7
P8M	5.6	3.5	18.9	9.0	41.0	45.5

Table 1: Determination of the chemical composition by ICP analysis of the manganese-zinc ferrite samples. The expected Zn, Mn and Fe weight contents are calculated assuming a stoichiometric $Zn_{1-x}Mn_xFe_2O_4$ with x = 0.2 and x = 0.8 phases.

The recorded XRD patterns confirm the formation of a pure spinel oxide (Figure 1) without any foreign phase. They match quite well with those tabulated for the *$Zn_{1-x}Mn_xFe_2O_4$ bulk solid solutions (ICDD n° 01-074-2398, 01-074-2399, 01-074-2400, 01-074-2401, 01-074-2402 for x = 0.1, 0.2, 0.4, 0.6, 0.8, respectively).* The considerable broadening of all diffraction peaks of the samples suggests that they are constituted by relatively small crystals. Indeed, Rietveld refinements permits us to estimate their average size at $<L_{XRD}>$ = 17 nm and their average micro-deformation at $<\varepsilon>$ = 0.2%. They also permit us to determine their cell parameter at a = 8.425(5) Å. surprisingly, there is no variation of the structural and microstructural parameters of the produced powders while the zinc content changes from one sample to another. Moreover, a net discrepancy is observed between the measured cell parameters and those expected for the stoichiometric $Zn_{1-x}Mn_xFe_2O_4$ x = 0.2 and 0.8 solid solutions, namely a = 8,4616 Å (ICDD n°01-074-2399) and a = 8,5136 Å (ICDD n°01-074-2402). The refined values are clearly out the expected Vegrad Law cell range. (the cell parameters of bulk $ZnFe_2O_4$ and $MnFe_2O_4$ are 8.44 and 8.54 Å, respectively [19]).

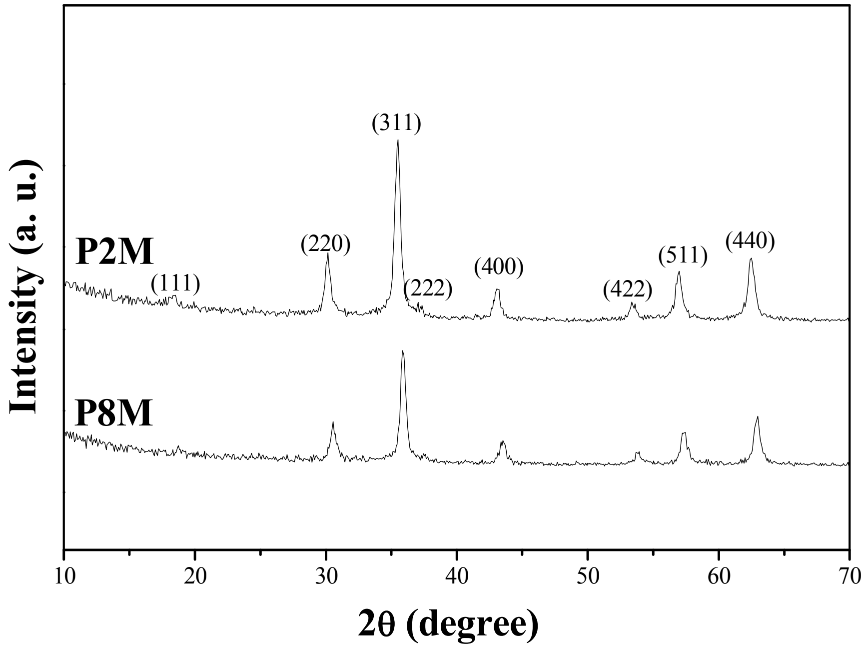

Figure 1: XRD patterns of P2M and P8M samples recorded in a θ-θ Bragg-Brentano configuration.

The XRD and ICP results suggest a metal deficiency in the unit cell and in turn deviation from stoichiometry. This spinel cation deficient structure might accommodate with oxygen vacancies to equilibrate between the total positive and negative charges of the spinel-like cation and anion sub-lattices, assuming manganese and iron cations as exactly divalent and trivalent cations, respectively. Or it might accommodate with an increase of the average oxidation state of its cations, mainly manganese ones, to compensate the total negative charge of the fully occupied spinel-like anion sub-lattice. In the two cases, the unit cell size decreases. In the first case, the solid oxide cohesion requires a unit cell contraction. In the second case, the average cation radius contraction decreases the cation-anion distances leading to the unit cell size reduction. The effect of the oxidation state change of the constituting atoms of an oxide phase on its stoichiometry and its unit cell size is something very often observed in solid state chemistry [20].

To pursue our investigations, we decided to carry out XPS experiments to characterize the electronic state of each constituting atom of these materials. Note XPS is a highly surface-specific technique. The information depth of XPS is considered to correspond to the sample thickness from which 95% of the detected signal originates. This depth is equal to $3\lambda \cos \theta$, where λ is the inelastic mean free path (IMFP) of the photoelectrons and θ the electron take-off angle with respect to the surface normal (equal to 0° in our setup). The inelastic mean free path of Fe2p photoelectrons was calculated using the Tougaard Quases-IMFP-TPP2M program which is based on the algorithm proposed by Tanuma, Powell, and Pen [21], and found equal to 1.6 nm, hence a depth analysis of *ca.* 4.8 nm. This value is lower than the crystal size inferred from Rietveld refinement (17 nm), but it is large enough to be considered quite deep to make the XPS analysis valuable and representative of the bulk composition of the studied nanocrystals.

Spectral calibration was determined by setting the main C1s component at 285 eV [22]. Figure 2 displays the XPS survey spectra of P2M and P8M samples. The main peaks are Mn2p, Fe2p, Zn2p, C1s and O1s centred at ca. 640, 720, 1030, 285 and 530 eV, respectively. The carbon signal (about 5 *wt*.-% carbon content) is mainly assigned to organic species, acetate and/or ethylene glycol, adsorbed on the surface of the particles.

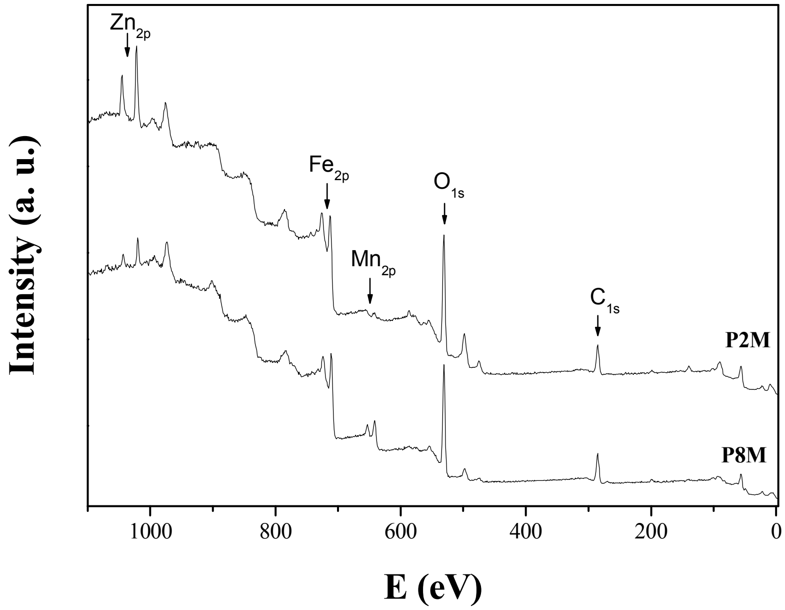

Figure 2: XPS survey spectra of P2M and P8M samples.

The other signals due to the mixed Mn-Zn ferrite particles appear to vary strongly in their intensity from one sample to another, particularly the Mn and Zn ones. Indeed, the comparison between the two spectra evidences clear modifications of the particle chemical composition when the nominal atomic Mn:Zn content changes. As expected, the Zn and Mn signal intensity increases and decreases, respectively, when the nominal zinc content increases, in agreement with the results obtained previously by chemical analysis.

Focusing now on the electronic state of each constituting cation, the high resolution spectra of the two studied samples were recorded. Fe2p signal, shown in Figure 3, is splitted into 2 main components, Fe2p$_{3/2}$ (at *ca.* 710 eV) and Fe2p$_{1/2}$ (at *ca.* 723 eV). with an intensity ratio, I(Fe2p$_{3/2}$)/I(Fe2p$_{1/2}$) of 2:1, as determined by fitting the whole Fe2p signal (see Figure 4 below). Each peak is mirrored by a shake-up satellite on its high binding energy side, caused by the configuration interaction due to relaxation of the valence electrons. The high peak widths indicate that Fe is found in two different oxidation states. Figure 3 allows comparing the Fe signal with reference samples, *i.e.* Fe_2O_3 (which contains Fe^{3+} ions only) and Fe_3O_4 (which contains a mixture of Fe^{2+} and

Fe^{3+} ions). It is clear that the Fe electronic states in the Mn-Zn ferrite particles are closer to those of Fe_3O_4 than Fe_2O_3: Fe thus appears to be in a mixed valence state, with the presence of both Fe^{2+} and Fe^{3+} ions. Considering the two oxidation states for Fe (Fe^{2+} and Fe^{3+}), and for each species, two main peaks ($Fe2p_{3/2}$ and $Fe2p_{1/2}$), each one accompanied by one shake-up, it is possible to fit the Fe signal with 8 components as illustrated in figure 4 for P8M sample. However, one has to remember that a characteristic feature of the oxide states is the multiplet splitting. It is caused by the interaction between the 2p electrons and the unpaired 3d electrons, and it results in a multitude of possible final states. The energy separation is usually so small that no discrete peaks will appear with a typical spectrometer resolution. Consequently, the multiplet splitting is seen in the spectrum as asymmetric broadening of the 2p peaks. The fitting parameters for the $Fe2p_{3/2}$ part of the Fe signal are summarized in Table 2. From the ratio of the relative intensity of the Fe^{2+} and Fe^{3+} $2p_{3/2}$ components (I/I_{Total}) against the whole $Fe2p_{3/2}$ signal ($\Sigma I/I_{Total}$), one can estimate the proportion of Fe^{2+} and Fe^{3+}, *i.e.*, 35 % and 65 %, respectively. This result must be underlined, because a small amount of Fe excess in the composition of ferrites by increasing the amount of Fe^{2+} ions can decrease the electrical resistivity and enhance electron hopping between Fe^{2+} and Fe^{3+} ions in the spinel unit cell. Reversely, a small amount of iron deficiency in the composition by reducing the amount of Fe^{2+} ions can increase the electrical resistivity and inhibit electron hopping between Fe^{2+} and Fe^{3+} ions.

The high resolution Mn2p spectra exhibits also two main peaks at *ca.* 640 ($2p_{3/2}$) and 655 ($2p_{1/2}$) eV. Satellite lines of manganese appear at much higher binding energies [23-25]. The Mn $2p_{3/2}$ lines, shown in figure 4 for P8M sample, are fitted with three peaks with binding energy at 640, 641.8 and 645.2 eV, assigned to Mn^{2+}, Mn^{3+} and Mn^{4+}, respectively. These binding energy values are in agreement with many reported XPS data of manganese containing compounds [23,26]. The Mn^{2+}, Mn^{3+} and Mn^{4+} atomic percent in the whole $Mn2p_{3/2}$ signal are of *ca.* 50 %, 40 % and 10 %, respectively, for all studied samples. Altogether, ICP and XPS results, suggest that the prepared Mn-Zn mixed ferrites exhibit a defect-spinel structure exhibiting a large deviation from stoichiometry with a none zero number of cation vacancies according the following chemical formula for each sample (see supporting information):

$$\left(Zn_{0.46}^{2+}Fe_{0.75}^{2+}Mn_{0.04}^{2+}\right)\left(Fe_{1.39}^{3+}Mn_{0.03}^{3+}Mn_{0.01}^{4+}\right)\ell_{\,0.32}O_4$$

and $\left(Zn_{0.14}^{2+}Fe_{0.77}^{2+}Mn_{0.22}^{2+}\right)\left(Fe_{1.44}^{3+}Mn_{0.18}^{3+}Mn_{0.04}^{4+}\right)\ell_{\,0.21}O_4$

where ℓ measures the deviation from stoichiometry.

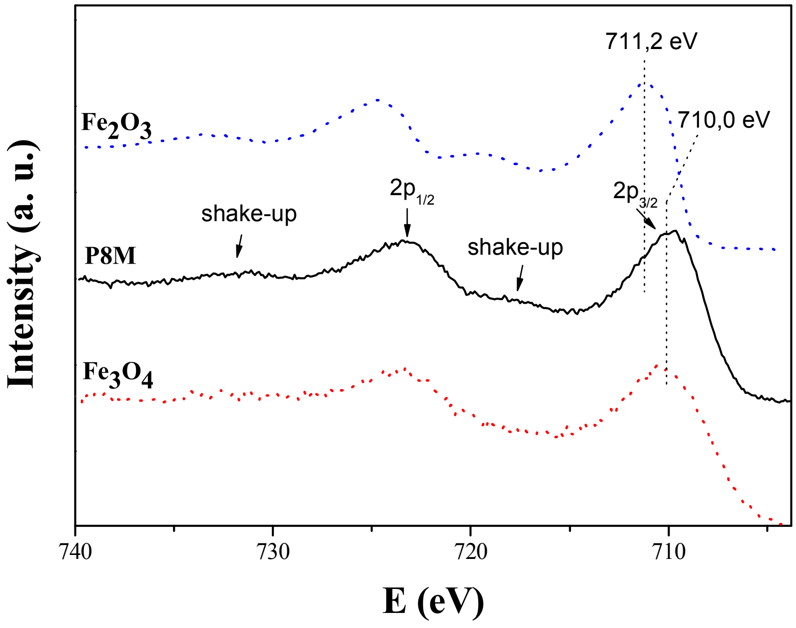

Figure 3. Comparison of the Fe XPS signal of P8M sample with that of reference compounds, *i.e.* Fe_2O_3 and Fe_3O_4.

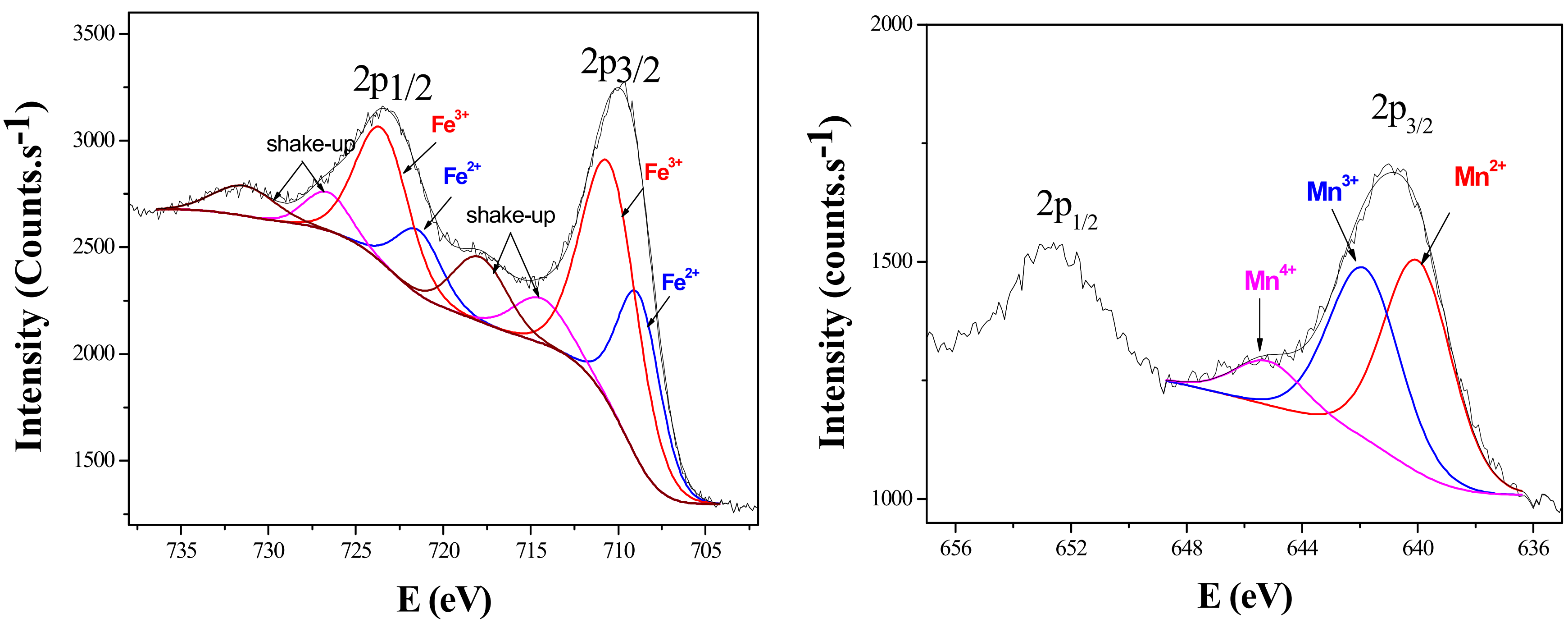

Figure 4. Peak-fitted Fe2p and Mn2p$_{3/2}$ core-line spectrum, respectively, of P8M sample. The colored solid lines are the peaks fitted to the experimental data.

	BE (eV)	*FWHM*	*L/G(%)*[a]	*I/Itotal*[b]
Fe^{2+} ($2p_{3/2}$)	708.8	3.0	30	0.18
Fe^{3+} ($2p_{3/2}$)	710.5	3.9	30	0.33
Fe^{2+} shake-up	714.4	3.7	0	0.06
Fe^{3+} shake-up	717.9	3.6	0	0.08
Mn^{2+} ($2p_{3/2}$)	640.0	2.9	30	0.27
Mn^{3+} ($2p_{3/2}$)	641.9	3.0	30	0.23
Mn^{4+} ($2p_{3/2}$)	645.2	2.9	30	0.06

[a] *The L/G parameter indicates the Lorentzian character in percentage in the Gaussian-Lorentzian function used to fit the spectra.*

[b] *I is the intensity of the fitted component while* I_{Total} *is the overall intensity of the analyzed signal: for Fe components,* I_{Total} *represents the sum of* $Fe2p_{3/2}$ *and* $Fe2p_{1/2}$ *signals while for Mn components,* I_{Total} *represents the sum of* $Mn2p_{3/2}$ *and* $Mn2p_{1/2}$ *signals.*

Table 2: The fitting parameters for the $Fe2p_{3/2}$ part of the XPS Fe signal of P8M sample

Such feature was already observed in manganese ferrite NPs prepared by other chemical routes. A cell parameter largely smaller than that expected for the $MnFe_2O_4$ stoichiometry was measured in particles prepared by co-precipitation [27,28] or by thermal decomposition of oxalates [29]. Similar results were obtained for manganese zinc ferrite NPs produced by reverse micelle route [30] or thermal decomposition of acetylacetonates [31]. In all the cases, the authors claimed that the spinel structure accommodates with cation vacancies in relation with a mixed valence state of Mn and/or Fe atoms. Clearly, the polyol process conducts to the production of ferrite particles with a defect spinel structure, cation vacancies being stabilized thanks to a valence state change of their constituting metallic cations.

Local structure. Important structural informations can be obtained from the measured cell parameters on these samples. Indeed, as previously mentioned, there is a basic correlation between the cell parameter value and the anion-cation distance for a particular site in the spinel structure. Tetrahedral and octahedral spinel sites are located at (1/8,1/8,1/8) and (1/2,1/2,1/2), respectively. The oxygen atom lies on the cube body diagonal at (*u*,*u*,*u*), where *u* is approximately 1/4. The cubic spinel structure thus has only two structural variables: (i) the unit-cell *a* and (ii) the oxygen positional parameter *u*. Assuming *u* to be equal 1/4, the *a* value can be completely determined using the following equation [32]:

$$a = 2.0995R_{tetra} + \sqrt{5.8182R_{octa}^2 - 1.4107R_{tetra}^2} \qquad (1)$$

where R_{tetra} and R_{octa} measure exactly the average value of the anion-cation distance on the tetrahedral and octahedral sites. They depend on both the oxidation state of the cations and their coordination, the covalent bonds in tetrahedral sites being shorter than electrovalent bonds in octahedral sites. The R_{tetra} and R_{octa} distances in Eq. (1) are calculated using the tabulated values of Mn-O, Fe-O and Zn-O [32-36] (see Table S1 in the supporting information section) considering various cation distributions and taking into account the previously obtained ICP and XPS results.

The calculated lattice parameter is then compared with the experimental one and the best concordance between the theoretical and the experimental *a* values determine the most realistic cations distribution in the solid solutions. We started our calculations assuming a thermodynamically stable structure in which the majority of ionic defects are located in the octahedral sites and the Mn^{2+}, Mn^{3+}, Mn^{4+}, Fe^{2+}, Fe^{3+} and Zn^{2+} cations are located in the site for which their stabilization energy in the related electrostatic field is the higher, agreeing thus with a strong Zn^{2+} tetrahedral coordination preference and a strong Fe^{2+}, Mn^{3+} and Mn^{4+} octahedral one, leading to a general formula:

$$\left[Mn_{1-u-v}^{2+}Zn_{u}^{2+}Fe_{v}^{3+}\right]\left(Fe_{2-v'-w-t-z}^{3+}Fe_{v'}^{2+}Mn_{w}^{3+}Mn_{t}^{4+}\ell_{z}\right)O_4$$

or $\left[Zn_{1-u}^{2+}Fe_{u}^{3+}\right]\left(Fe_{2-v-y-w-t-z}^{3+}Fe_{v}^{2+}Mn_{y}^{2+}Mn_{w}^{3+}Mn_{t}^{4+}\ell_{z}\right)O_4$

where the brackets correspond to the tetrahedral sites and parentheses to the octahedral ones, and ℓ the deviation from stoichiometry. For P2M sample, the calculation of the cell parameter in both configurations gives exactly the same result, namely a = 8.45 ± 0.02 Å. This is not so surprising in regard to its very weak Mn content and obviously Mn^{2+} one. A displacement of divalent manganese cations from octahedral to tetrahedral sites does not affect significantly the *a* value. For P8M sample, there is a marked difference between the two configurations, the former giving the closest *a* value to that inferred from Riteveld refinements, meaning that the cation distribution in this sample agrees with Zn^{2+} and Mn^{2+} tetrahedral coordination preference and a Fe^{2+} octahedral one. Anyway, in all the cases, a partial transfer of Zn^{2+} from tetrahedral to octahedral sites and a reverse transfer of Fe^{3+} lead to a progressive increase of the theoretical *a* value. Similarly, a transfer of the cation vacancies from the octahedral to the tetrahedral sites, accompanied with a decrease of the concentration of the Fe^{3+} ions in these sites leads also to a significant *a* value increase.

To confirm this cation distribution toward the spinel lattice, EXAFS experiments were carried out. The moduli of the Fourier transform (FT) of the total EXAFS data for the different samples are given in figure 5 at the Fe and Zn K-edges. The plot of the moduli of the FT is not corrected from the electron phase shift. It is related to the radial distribution function of back-scatterers around the absorbing atoms. By comparison with that of standard $ZnFe_2O_4$ and Fe_3O_4, which adopt a normal and inversed spinel structure, respectively, it is possible to identify the main FT-peaks, at the Zn and Fe K-edges. For all the samples, the FT profile at Fe, and Zn K-edges suggested that iron ions occupy both tetrahedral (A) and octahedral (B) sites while zinc ones are located in tetrahedral sites only. Indeed, at the Fe K-edge, the relative intensity of the two peaks centered at 2.7 and 3.2 Å. These FT peak positions corrected from the electron phase shift which is about 0.3-0.4 Å measure the distances between the Fe ions and their second nearest metallic neighbors. They are close to those of standard Fe_3O_4, where the third of iron ions is tetrahedrally coordinated and the other two thirds are octahedrally coordinated, EXAFS analysis being not efficient to distinguish between the different oxidation states, +2 and +3, of iron atoms. At the Zn K-edge, a great proximity between the overall FT profiles of the two samples and the standard $ZnFe_2O_4$, where zinc cations occupy exclusively tetrahedral sites, is observed. The loss of intensity of the peak centered at 3.1 Å in the nanoparticles, corresponding to the distance between the Zn ions and their second nearest metallic neighbors, might be assumed to be due to their nanocrystalline character, the surface zinc ions of the particles having nearest metallic neighbors on one side none on the other side [37]. Such feature is often observed in the case of metal nanoparticles and used to solve their 3D structure [38].

Anyway, we performed least square modeling using single scattering Fe and Zn EXAFS simulation on the first filtered Fe and Zn FT peak corresponding to the Fe-O and Zn-O shells, respectively, to determine the local symmetry of these cations. The fitting procedure is based on the equation [17]:

$$k\ \chi(k) = \sum_i \frac{N_i}{R_i^2} \exp(-2k^2\sigma_i^2)\exp(-\frac{2R_i}{\lambda(k})\left|f_i(\pi,k)\right|.\sin(2kR_i + \Phi_i(k)) \qquad (2)$$

where k is the wave vector, $\chi(k)$ the EXAFS function, N_i is the number of back-scatterers “i” at a distance R_i from the central atom and σ_i the Gaussian Debye-Waller factor associated with R_i. The energy threshold, E_0, taken at the first inflexion of the absorption edge is corrected in the fitting procedure by the ΔE_0 parameter. $|f_i(\pi,k)|$, and, $\Phi_i(k)$, are the amplitude and phase shift functions, respectively.

Two contributions have been necessary to reproduce the experimental EXAFS data, at the Fe K-edge, while only one has been used to simulate the experimental EXAFS signal, at the Zn K-edge (the quality of the fits is illustrated in figure S2 in the supporting information section for P8M sample). The main structural fitted parameters are listed in table 3. The refined interatomic cation-oxygen distances are consistent with the tabulated ones, for tetrahedraly coordinated zinc cations and for tetrahedrally and octahedrally coordinated iron ones (see Table S1). Using the fitted coordination numbers N of Fe and Zn, the uncertainties being estimated to be about 15% [17], it is possible to determine the occupancies of Fe and Zn cations in A sites, expressed in % of the total Fe and Zn cations, respectively. They are found to be about 24 and 28% for Fe and 100 and 100 % for Zn, in P2M and P8M samples, respectively.

At the Mn K-edge, such quantitative analysis of the EXAFS data is not easy. In one hand, the energy range of Mn K-edge spectra are drastically shortened, due to the recovering with the Fe K-edge X-ray absorption signal. In other hand, EXAFS analysis is not always efficient to distinguish between the different manganese oxidation states +2, +3 and +4, particularly if their related distances to oxygen ions in tetrahedral and/or octahedral polyhedra are close to each other. Nevertheless, the moduli of the FT at the Mn K-edge of the two samples, are almost identical and exhibit a first peak, corresponding to Mn-O interatomic distances, which is dedoubled. Such feature is associated with two Mn-O distances, a short one and a long one. Indeed, the peaks in the FT moduli of the total EXAFS function weighted by k^3, reported in Figure 5, correspond to apparent interatomic distances. Two first peaks mean two distinct nn Mn-O shells for the nearest nn neigbor. Considering the listed distances in the supporting information section (Table S1), one can attribute the shortest and the longest distances to the octahedral Mn^{4+}-O^{2-} and Mn^{2+}-O^{2-} atomic pairs, respectively. A third distance, an intermediate one comprised between the two previous ones, exists and corresponds indifferently to the octahedral Mn^{3+}-O^{2-} and tetrahedral Mn^{2+}-O^{2-} atomic pairs. Comparing the relative intensity of the two corresponding Mn-O FT-peaks, one may assume that the Mn-O distances are quite equivalently distributed between short, medium and long ones in P2M, while they are in majority short or medium in P8M. Using all these information, we can propose a probable cation distribution fixing first the localization of Fe^{2+}, Mn^{3+} and Mn^{4+} cations as well as the vacancies in the octahedral sites, Zn^{2+} in the tetrahedral ones and Fe^{3+} in both octahedral and tetrahedral ones.

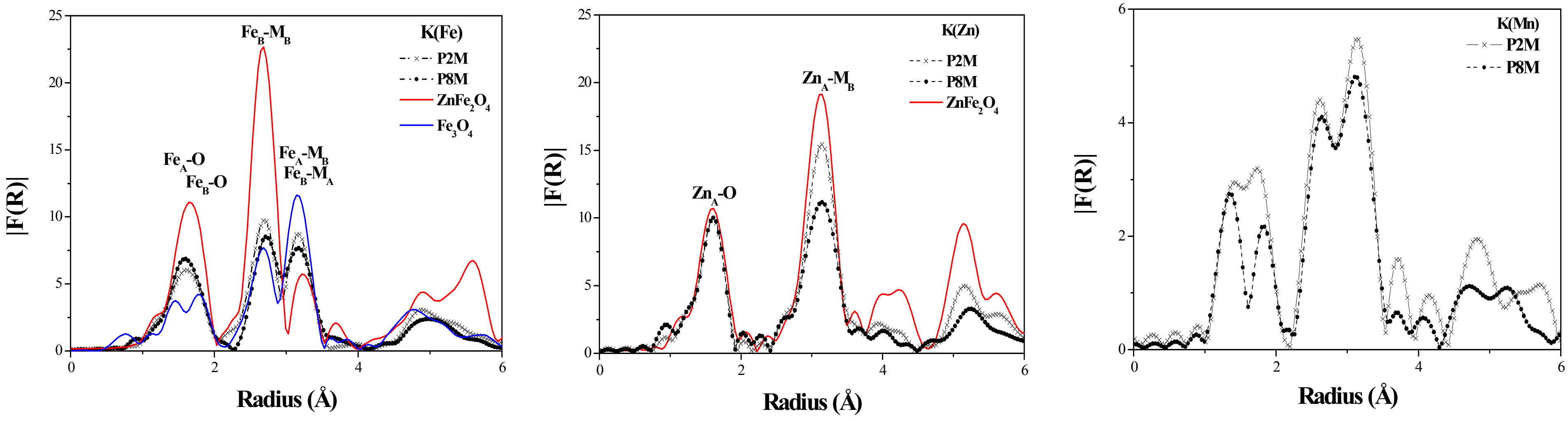

Figure 5. Mn, Fe and Zn K-edges Moduli of the FT experimental EXAFS signals of P2M and P8M samples, compared to that of bulk $ZnFe_2O_4$ and Fe_3O_4. The A and B indices correspond to the tetrahedral and octahedral spinel sites occupancy respectively. M corresponds to the metallic second nearest neighbours.

		K(Fe)				K(Zn)			
Sample	First shell	Fe_A-O	Fe_B-O	ρ (%)	[Fe_A/Fe] (%)	Zn_A-O	Zn_B-O	ρ (%)	[Zn_A/Zn] (%)
P2M	N	0.98	4.52	0.8	24	3.94	0.00	0.3	100
	R (Å)	1.93	2.02			1.97	--		
	σ (Å)	0.058	0.088			0.059	0.00		
	ΔE_0(eV)	13.1	9.8			4.7	0.00		
P8M	N	1.10	4.36	0.6	28	4.02	0.00	0.9	100
	R (Å)	1.93	2.02			1.97	--		
	σ (Å)	0.047	0.086			0.063	0.00		
	ΔE_0(eV)	16.1	9.1			3.5	0.00		

Table 3. EXAFS results at the Fe and Zn K-edges of the P2M and P8M samples, where ρ the residue measures the quality. It must be the smallest possible. The [Fe_A/Fe] and [Zn_A/Zn] parameters correspond to the ratio of tetrahedrally coordinated Fe and Zn cations, respectively.

Starting from these assumptions, it becomes possible to share Mn^{2+} cations between the two types of sites, the content of all tetrahedrally coordinated cations and that of all octahedrally coordinated ones, including vacancies, leading to a value of 1.00 and 2.00 per formula unit, respectively:

$\left[Mn^{2+}_{0.04}Zn^{2+}_{0.46}Fe^{3+}_{0.50}\right]\left(Fe^{3+}_{0.89}Fe^{2+}_{0.75}Mn^{3+}_{0.03}Mn^{4+}_{0.01}\ell_{0.32}\right)O_4$ for P2M

and $\left[Mn^{2+}_{0.22}Zn^{2+}_{0.14}Fe^{3+}_{0.64}\right]\left(Fe^{3+}_{0.80}Fe^{2+}_{0.77}Mn^{3+}_{0.18}Mn^{4+}_{0.04}\ell_{0.21}\right)O_4$ for P8M

Microstructural properties. The TEM images showed that the ferrite particles are isotropic in shape and very uniform in size (Figure 6), with an average diameter varying from 78±15 to 29±4 nm by changing the nominal atomic Mn:Zn ratio from 20:80 to 80:20 (see Figure S3 in the supporting information section), evidencing a size dependency to the zinc content.

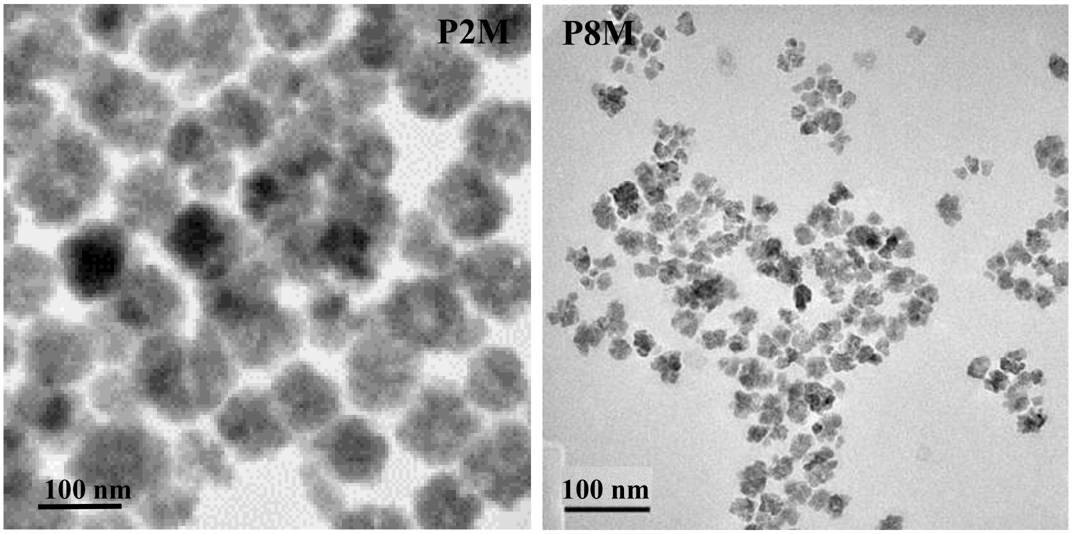

Figure 6. TEM images of an assembly of P8M and P2M particles.

A zoom on a representative particle from of each sample shows (Figure 7) that it consists of a given number of smaller in size nanocrystals (less than 10 nm). Moreover, their fast Fourier transformation (FFT) patterns (Figure 7) are of Laüe type. This means that they are textured polycrystals or pseudo-single crystals, justifying thus the measured discrepancy between the measured TEM and XRD sizes. Such a feature was already observed for different oxide particles produced in polyol [39]. All these results suggest that the particle formation in polyol is driven by an aggregation growth mechanism.

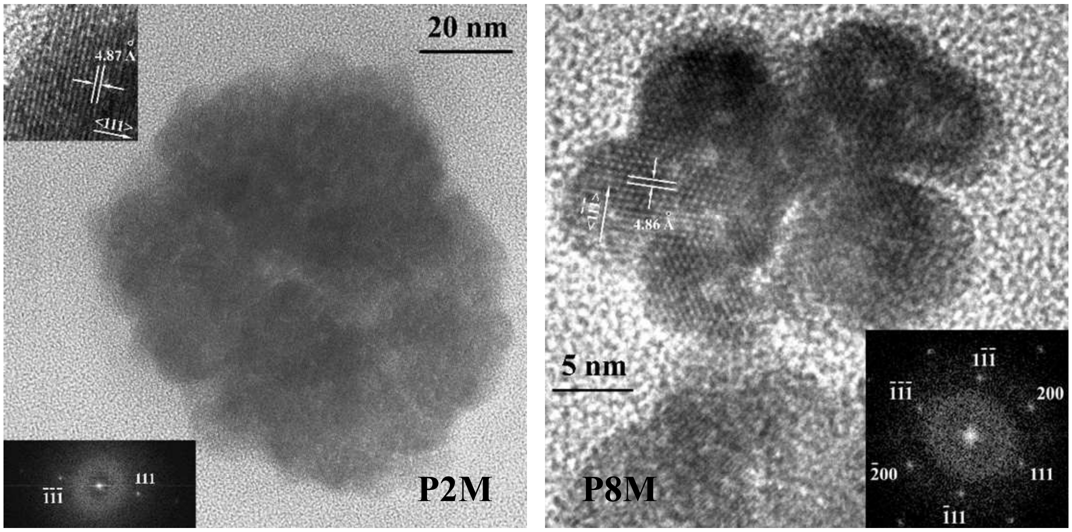

Figure 7. Zoom images on representative particle of each sample and its FFT patterns indexed in the spinel structure. Note the double (400) reflections introduce the normally forbidden (200) reflections observed for P8M sample.

The size variation between the zinc poorest and richest polycrystals is very probably related to the variation of the number of nuclei. The largest polycrystals correspond to the coalescence of a greater number of primary particles and then to the formation in the reaction medium of a greater number of nuclei, and reversely, the smallest polycrystals correspond to the coalescence of a smaller number of primary particles and then to the formation in the reaction medium of a smaller number of nuclei. This is not so surprising. Indeed, it is usually considered that the energy barrier for the formation of $ZnFe_2O_4$ is much lower than that of $MnFe_2O_4$ because of the zinc ion's strong preference for tetrahedral sites. The main consequence is that the nucleation energy of $ZnFe_2O_4$ or $Mn_{1-x}Zn_xFe_2O_4$ x ~ 1 crystals is smaller than that of $MnFe_2O_4$ or $Mn_{1-x}Zn_xFe_2O_4$ x ~0 [40,41], leading to a higher nuclei number

Redox and catalytic activity evaluation. Before testing the produced Mn-Zn ferrite NPs for catalytic DME combustion, H_2-TPR and O_2-TPD characterizations were made to study their redox activities, and the results are shown in Figure 8 and Table 4. Clearly, the two samples exhibit three overlapped TPR peaks related to the reduction of Mn^{4+} into Mn^{3+} and Mn^{2+} and Fe^{3+} into Fe^{2+} or even Fe as already observed in manganese and manganese-zinc ferrite NPs produced by other routes [41], confirming the mixed valence state of Mn and Fe atoms in the studied systems. P2M appears to be more easily reduced than P8M. It consumes more hydrogen (12.33 mmol/g) than P8M (11.36 mmol/g), meaning that the average oxidation state of its constituting metal cations (Fe, Mn and Zn) is higher than that in its P8M parent. Concerning the O_2-TPD profiles, once again three oxygen desorption peaks are observed. They are located at around ~100°C, 200-450° and ~600°C and are assigned to the physisorption of oxygen (α peak), its weak chemisorption (suprafacial oxygen, β peak) and its strong chemisorption (lattice oxygen, γ peak), respectively [42]. P2M exhibits a more marked β peak than P8M, suggesting its higher oxidation activity. Note the carried out pretreatment for TPR and TPD experiments were realized under insert atmosphere at a temperature (350°C and 200°C, respectively) lower than the required one for the first reduction or oxidation reaction in these particles, making the previously described TPR and TPD results significantly representative of the intrinsic redox behavior of the as-produced NPs. Dimethyl ether (DME) is a kind of environmental energy with multi-sources and multi-purpose.

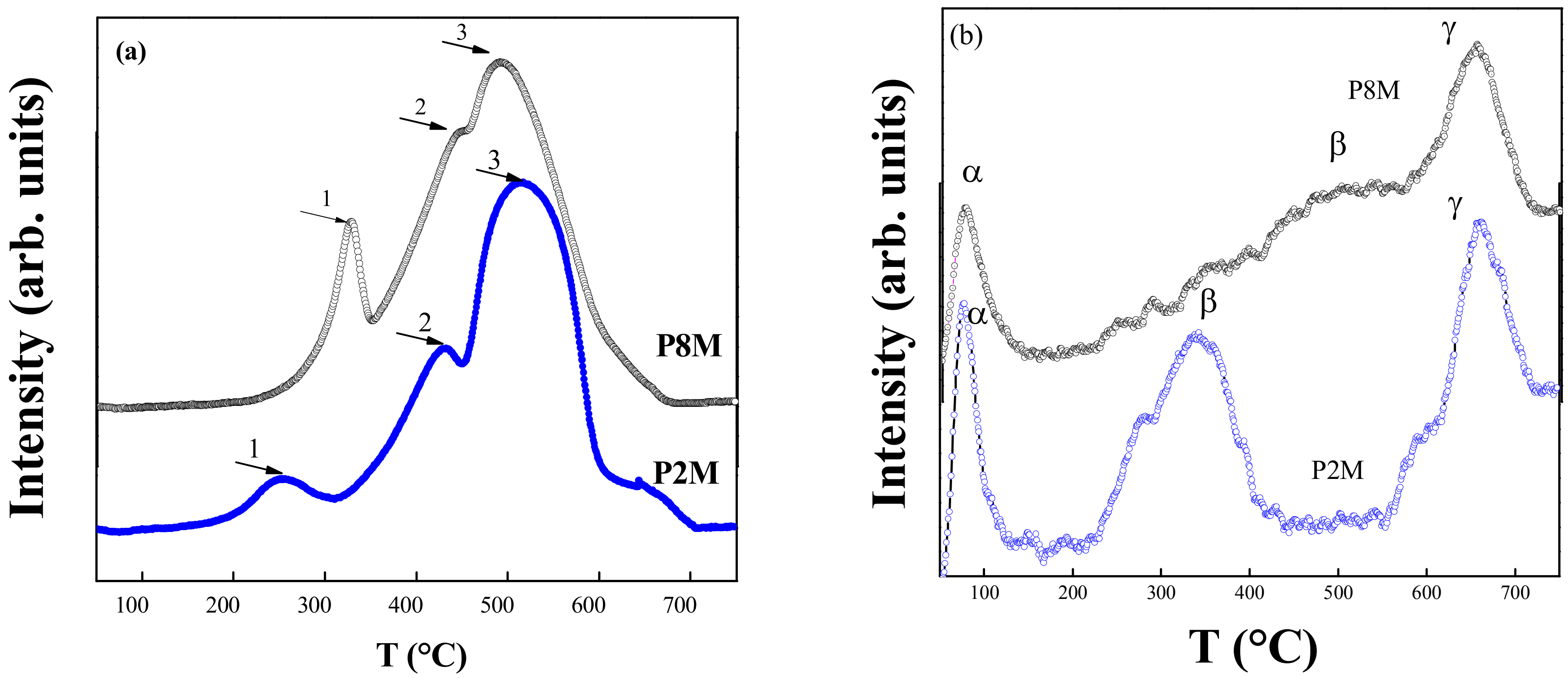

Figure 8. H_2-TPR (a) and O_2-TPD (b) plots of P8M and P2M samples.

	H_2 consumption					
	Peak 1		Peak 2		Peak 3	
	T (°C)	n (mmol/g)	T (°C)	n (mmol/g)	T (°C)	n (mmol/g)
P8M	328	1.50	456	3.28	490	6.58
P2M	255	0.85	431	2.93	516	8.55

	O_2 release					
	Peak α		Peak β		Peak γ	
	T (°C)	n (mmol/g)	T (°C)	n (mmol/g)	T (°C)	n (mmol/g)
P8M	76.6	0.121	-	-	655	0.193
P2M	76.5	0.106	342.5	0.235	662	0.122

Noted: Overlapped peaks were separated by fitting the curves to data using the software of AutoChem II .

Table 4. Results of H_2-TPR and O_2-TPD experiments for P8M and P2M samples.

To increase combustion efficiency and decrease the emission of hydrocarbons, catalytic combustion of DME is often considered when it is used as fuel. Several catalyst systems have been reported, *eg*, noble metal (Pd, Rh, Pt) [43], hexaaluminate [44], and manganese oxides [45]. From the point view of practical application, the transition metal oxides hold great potential for DME combustion because of their low-cost and relatively high activity. As for ferrite catalysts, they are reported as effective catalysts for catalytic combustion of toluene [46] and of ~~for~~ DME [47]. Here, we explored the catalytic combustion of DME over the polyol prepared ferrites. GC analysis confirms that the combustion is total according the selected working conditions. No other products than CO_2 and H_2O are formed. The combustion activity of P2M is a little superior than that of P8M (Figure 9). For P2M sample, the T_{10} and T_{90} are 257 °C and 276 °C, respectively. However, the P8M sample has a T_{10} of 243 °C and a T_{90} of 291°C (Figure 8). The catalytic performance (T_{10} = 257 °C and T_{90}= 276 °C at SV = 10.2 $L.g^{-1}_{cat}.h^{-1}$) over P2M sample is better than that (T_{50} = 356 °C and T_{90}= 409 °C) over cobalt ferrite [47], that (T_{10} = 170 °C and T_{90}= 370 °C) over $BaNi_{0.2}Mn_{0.8}Al_{11}O_{19-\delta}$ [44], that (T_{10} = 106 °C and T_{90}> 320 °C) over Pd/Al_2O_3 [43a], but similar to or inferior to that

(T_{10} = 184 °C and T_{90}= 220 °C) over α-MnO_2 [45b], that (T_{10} = 171 °C and T_{90}= 180°C) over Cu-OMS-2 [45a], that (T_{10} = 149 °C and T_{90}= 159 °C) over Ce-OMS-2 [45c].

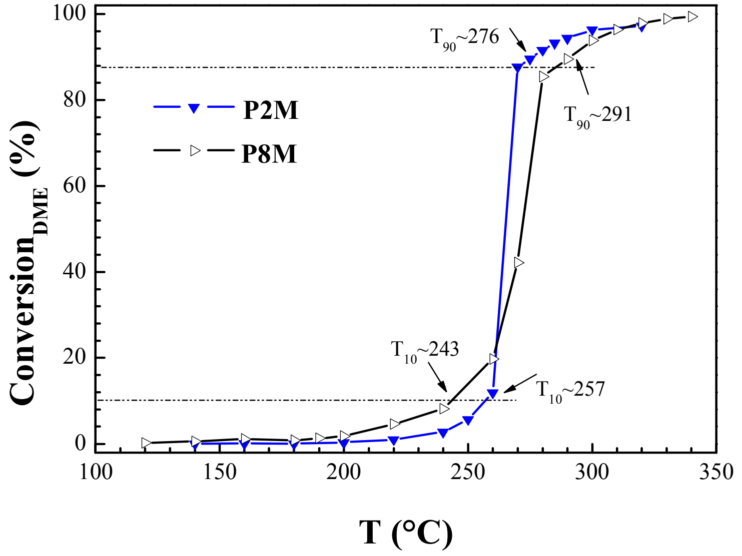

Figure 9. DME conversion as a function of the temperature for P8M and P2M samples.

Note the homogeneous combustion of DME, under the same reaction conditions and without catalysts, is efficiently achieved only at a temperature higher than 525 °C (see Figure S4 in the supporting information section), largely higher than that required in presence of P2M or P8M powders. These results must be underlined, they unambiguously evidence the catalytic activity of the polyol-made non-stoichiometric manganese-zinc ferrite NPs toward DME combustion.

DISCUSSION

It appears clearly that the synthetic procedure developed in the present study offers several important advantageous features for the synthesis of nanoscaled manganese-zinc ferrite powders. First, the synthetic process is economical, because it involves inexpensive metallic salts (chloride and acetate) and need moderate heating (160-170

°C). Second, the particles are directly produced as stable vacancy-deficient ferrites, as established by XRD, XPS and ICP analyses, without going through a supplementary appropriate heat treatment at oxidizing atmosphere, as it is often the case when this kind of material is desired. Third, the ferrite nanoparticles are obtained with a local structure as close as possible to their bulk counterparts, while, in the majority of the cases, a redistribution of cations towards equilibrium conditions are observed only after a prolonged annealing treatment. Finally, they exhibit a high crystalline quality and a fine microstructure, as observed by TEM and HRTEM, which is of primary importance for the desired application.

Catalytic tests consisting on DME combustion have shown that the produced ferrite particles exhibit interesting catalytic feature, the manganese poor sample (P2M) being more reactive than its manganese rich counterpart (P8M), while the former exhibits a larger particle size than the latter (78 vs. 29 nm), suggesting that the particle size is not the dominant factor affecting the DME combustion. This may be explained by the fact that the crystal size remains almost equivalent in both samples (8-10 nm) according to the HRTEM observations. In the same time, the structure doesn’t appear to be a limiting parameter since both spinel-like sample exhibit a cation distribution close to the thermodynamically stable one, namely Fe^{2+}, Mn^{3+} and Mn^{4+} octahedral and Zn^{2+} tetrahedral coordination preference, respectively. Moreover, focusing on octahedrally coordinated iron cations, EXAFS analysis shows that their atomic ratios in both samples, P2M and P8M, are very close to each other (76 vs. 72 at.-%), making the contribution of the structural parameter toward the catalytic combustion activity of the two samples quite equivalent. Note, the atomic ratio of octahedrally coordinated manganese cations was also calculated for each sample, assuming, as a first approximation, that Mn^{2+} cations are exclusively localized in tetrahedral spinel sites. The obtained values are 67 vs. 50 at.-% for P2M and P8M, respectively. The difference between the two samples is more marked here, but at this stage of our structural analysis, it is not easy to conclude, since the manganese content of P2M is very week (about 2% of the total cation amount), making this sample closest to a non-stoichiometric zinc ferrite than a manganese-zinc ferrite. On these bases, one may suppose that the improved catalytic behavior of P2M can be due to its own chemical composition, namely to its close to zero manganese content. In the same time, looking at the relevant literature, manganese, cobalt and manganese-cobalt ferrite NPs are more often cited as good redox catalysts, including DME combustion catalysts, than zinc ferrite ones [46,48], making this hypothesis irrelevant.

Normally, local defects are very important for redox solid catalysts. The stabilization of metal cations in a mixed valence state into the spinel lattice induces deviation from stoichiometry and the creation of cation vacancies, ℓ, with respect to the cation and anion charge balance. This deviation from the perfect spinel structure corresponds to about 0.3 and 0.2 vacancies per formula unit in P2M and P8M, respectively, slightly more important in the former than in the latter. Their relative catalytic activity is giving thus a slight advantage to the former.

Finally, reducibility is an important parameter to evaluate the redox activity which is directly related with the catalytic activity. The TPR tests show that P2M powder reveals a greater susceptibility to the reduction with a higher hydrogen consumption than that of P8M. A higher hydrogen consumption means its average oxidation state is also higher, which is thought to be helpful for catalytic activity [50]. The TPR results are consistent with the catalytic performance. In parallel, the amount of desorbed oxygen and the temperature at which oxygen is desorbed are thought to be directed related with the capability to form surface vacancies, and are often considered to be a key factor determining the catalytic activity [51]. Based on the TPD tests, the P2M sample possesses more weakly chemisorbed oxygen than that of P8M sample, and this is in accordance with their T_{90} order. Moreover, the suprafacial oxygen species over the spinel ferrite dominates its catalytic activity.

CONCLUSION

Nanosized manganese-zinc spinel ferrite powders have been synthesized from manganese, zinc and iron salts in ethyleneglycol through a forced hydrolysis reaction. XRD, XPS and EXAFS analysis show that the polyol-made crystals are defect spinel ferrites in which iron and manganese cations are present in a mixed valence state. Their local structure, in terms of cation distribution among the spinel lattice, respects the octahedral and tetrahedral crystal field preference of Fe^{2+}, Mn^{3+}, Mn^{4+} and Zn^{2+}, respectively. The increase in the Mn oxidation state (+3 for the most part) affects also the unit cell size, which is found to be smaller than that expected in stoichiometric bulk $Zn_{1-x}Mn_xFe_2O_4$. TEM and HRTEM analyses show that the particles are polycrystalline and highly crystallized, isotropic in shape, with an average diameter lying in the nanometer range, increasing with the Zn concentration. Moreover, they exhibit a pseudo-single crystal behavior thanks to the texturation of their constituting nanocrystals, making them particularly valuable as heterogeneous catalysts. Preliminary solid-gas catalysis tests have shown that the manganese poor sample exhibits a superior activity for DME combustion than its manganese rich counterpart, due to its better redox activity in relation to its more important stoichiometry deviation.

ACKNOWLEDGMENT.

They want to acknowledge Dr. Gilberto Vlaic and Dr Luca Olivi from the ELLETRA synchrotron ring of Trieste for their help during EXAFS experiments. They want also to acknowledge Dr. Patricia Beaunier for her technical support during TEM observations at the Pierre & Marie Curie University in Paris.

REFERENCES

1 a) R. Lebourgeois, *Ferrites faibles pertes pour applications fréquentielles, in Techniques de l'Ingénieur, Traité d'électronique, E1, Les Techniques de l'Ingénieur*, (2000) pp. E1.760-1-E1.760-.0 ; b) S. Smith, H.P.J. Wijn, *Ferrites: Physical Properties of Ferrimagnetic Oxides in Relation to Their Technical Applications*, pp. 369, Publisher: John Wiley & Sons, New York (1959)

1. a) Z. Beji A. Hanini, L.S. Smiri, J. Gavard, K. Kacem, F. Villain|, J.M. Grenèche, F. Chau, S. Ammar, *Magnetic properties of Zn-substituted $MnFe_2O_4$ nanoparticles synthesized in polyol as potential heating agents for hyperthermia. Evaluation of their toxicity on Endothelial cells*, Chem. Mater. (2010) 22[19], pp 5420-5429 ; b) C. Bárcena, A.K. Sra, G. . Chaubey, C. Khemtong, J. Ping Liu, J. Gao, *Zinc ferrite nanoparticles as MRI contrast agents*, Chem. Comm. (2008) pp. 2224-2226.

3 C.W. Lim, I.S. Lee, *Magnetically recyclable nanocatalyst systems for the organic reactions*, Nano Today (2010) 5, pp. 412-434.

4 W.F. Shangguan, Y. Teraoka, S. Kagawa, *Promotion effect of potassium on the catalytic property of $CuFe_2O_4$ for the simultaneous removal of NOx and diesel soot particulate*, Appl. Catalysis B (1998) 16[2], pp.149-154.

5 a) M. Estrella, L. Barrio, G. Zhou, X. Wang, Q. Wang, W. Wen, J.C. Hanson, A.I. Frenkel, J.A. Rodriguez, *In Situ Characterization of $CuFe_2O_4$ and Cu/Fe_3O_4 Water−Gas Shift Catalysts*, J. Phys. Chem. C (2009) 113[32], pp. 14411-14417 ; b) V. Subramanian, E. S. Gnanakumar, D.W. Jeong, W.B. Han, C.S. Gopinath, H.S. Roh, *A rationally designed $CuFe_2O_4$-mesoporous Al_2O_3 composite towards stable performance of high temperature water–gas shift reaction*, Chem. Commun. (2013) 49, pp. 11257-11259.

6 K. Faungnawakij, N. Shimoda, T. Fukunaga, R. Kikuchi, K. Eguchi, *Crystal structure and surface species of $CuFe_2O_4$ spinel catalysts in steam reforming of dimethyl ether*, Appl. Catal. B (2009) 92[3], pp. 341-350.

7 A. Abbaspour, E. Mirahmadi, *Electrocatalytic hydrogen evolution reaction on carbon paste electrode modified with Ni ferrite nanoparticles*, Fuel (2013) 104, pp. 575-582.

8 L. Wang, H.Y. He, *Surface alkaline-acidic characteristics and photo catalytic properties of* $Co_{1-x}Zn_xFe_2O_4$ *nano-particles synthesized by hydrothermal method*, J. Sci. Res. Rep. (2014) 3[2], pp. 263-274.

9 S. Bhukal, S. Bansal, S. Singhal, *Magnetic Mn substituted cobalt zinc ferrite systems. Structural, electrical and magnetic properties and their role in photo-catalytic degradation of methyl orange azo dye*, Physica B: Condens. Matter (2014) 445[], pp. 48-55.

10 a) J.S. Kim, J.R. Ahn, *Characterization of wet processed (Ni, Zn)-ferrites for* CO_2 *decomposition,* J. Mater. Sci. (2001) 36[19], pp 4813-4816 ; b) S. Komarneni, M. Tsuji, Y. Wada, Y. Tamaura, *Nanophase ferrites for* CO_2 *Greenhouse-gas decomposition*, J. Mater. Chem. (1997) 7[12], pp. 2339-2340 ; c) J.S. Kim, J.R. Ahn, C. Woo Lee, Y. Murakami, D. Shindo, *Morphological properties of ultra-fine (Ni,Zn)-ferrites and their ability to decompose* CO_2, J. Mater. Chem. (2001) 11[12], pp. 3373-3376.

11 E. Kester, P. Perriat, B. Gillot, P. Tailhades, A. Rousset, *Correlation between oxidation states of transition metal ions and variation of the coercivity in mixed-valence defect spinel ferrites*, Solid State Ionics (1997) 101-103[Part 1], pp. 457-463.

12 B. Gillot, *DTG curves of selective oxidation of submicrometer mixed valency spinels: data table for the oxidation temperature of transition metals and its relation to the cation-oxygen distance*, J. Solid State Chem. (1994) 113[1], pp. 163-167.

13 L. Poul, S. Ammar, N. Jouini, F. Fiévet, F. Villain, *Synthesis of Inorganic Compounds (Metal, Oxide and Hydroxide) in Polyol Medium: A Versatile Route Related to the Sol-Gel Process*, J. Sol-Gel Sci. Technol. (2003) 26[1-3], pp. 261-265.

14 a) T. Rhadfi, J.Y. Piquemal, L. Sicard, F. Herbst, E. Briot, M. Benedetti, A. Atlamsani, Polyol-made Mn_3O_4 nanocrystals as efficient Fenton-like catalysts, Appl.

Catalysis A (2010) 386[1-2], pp. 132–139 ; b) T. Rhadfi, L. Sicard, F. Testard, O. Tache, A. Atlamsani, E. Anxolabehere-Mallart, Y. Le Du, L. Binet, J.Y. Piquemal, *A Comprehensive Study of the Mechanism of Formation of Polyol-Made Hausmannite Nanoparticles: from Molecular Reactions to Solid Precipitation*, J. Phys. Chem. C (2012) 116[9], pp. 5516-5523.

15 a) H. Basti, L. Ben Tahar, L.S. Smiri, F. Herbst, M.J. Vaulay, F. Chau, S. Ammar, S. Benderbous. *Catechol Derivatives-Coated* Fe_3O_4 *and* γ-Fe_2O_3 *Nanoparticles as Potential MRI Contrast Agents.* J. Colloid Interface Sci. (2010) 341[2], pp. 248-254 ; b) L. Poul, S. Ammar, N. Jouini, F. Fiévet, F. Villain, *Metastable solid solutions in the system ZnO-CoO: synthesis by hydrolysis in polyol medium and study of the morphological characteristics,* Solid State Sci. (2001) 3[1-2], pp. 31-42.

16 L. Lutterotti, S. Matthies, H.R. Wenk, *MAUD: a friendly Java program for material analysis using diffraction,* IUCr: Newsletter of the CPD (1999) 21, pp. 14-15.

17 M. Newville, *IFEFFIT : interactive XAFS analysis and FEFF fitting*, J. Synchrotron Rad. (2001) 8[Part 2], pp. 322-324.

18 J. Mustre de Leon, J.J .Rehr, S.I. Zabinsky,d R. C. Albers, *Ab initio* curved-wave X-ray-absorption fine structure, Phys. Rev. B (1991) 44 [9], pp. 4146-4156.

19 F.S. Galasso, *Structure and Properties of Inorganic Solids*, In: International Series of Monographs in Solid State Physics, Publisher: Pergamon Press, Oxford, Vol. 7, pp. 296 (1970).

20 a) A. Delmastro, D. Mazzaa, S. Ronchetti, M. Vallino, R. Spinicci, P. Brovetto, M. Salis, *Synthesis and characterization of non-stoichiometric* $LaFeO_3$ *perovskite*, Mater. Sci. Eng. B (2001) 79[2], pp. 140-145 ; b) A. Anspoks, A. Kalinko, R. Kalendarev, A. Kuzmin, *Local structure relaxation in nanocrystalline* $Ni_{1-x}O$ *thin films*, Thin Solid Films (2014) 553, pp. 58-62 ; c) L. Wu, H.J. Wiesmann, A.R. Moodenbaugh, R.F. Klie, Y. Zhu, D.O. Welch, M. Suenaga, *Oxidation state and lattice expansion of* CeO_{2-x} *nanoparticles as a function of particle size*, Phys. Rev. B

(2004) 69, pp. 125415.1-125415.9 ; d) Y. Regaieg, F. Ayadi, S. Nowak, M. Koubaa, A. Cheikhrouhou, S. Reguer, J. Monnier, L. Sicard, S. Ammar-Merah, *Magnetocaloric properties of* $La_{0.67}Ca_{0.33}MnO_3$ *produced by reactive spark plasma sintering and by conventional ceramic route,* Mater. Res. Express, (2014) 1, pp. 046105.1- 046105.6.

21 S. Tanuma, C.J. Powell, D.R. Penn, *Calculations of electron inelastic mean free paths. V. Data for 14 organic compounds over the 50–2000 eV range,* Surf. Interface Anal. (1993), 21[3], pp. 165–176.

22 G. Beamson, D. Briggs, *High-resolution monochromated X-ray photoelectron spectroscopy of organic polymers: a comparison between solid-state data for organic polymers and gas-phase data for small molecules*, Mol. Phys. (1992) 76[4], pp. 919-936.

23 C. Drouet, C. Laberty, J.L.G. Fierro, P. Alphonse, A. Rousset, *X-ray photoelectron spectroscopic study of non-stoichiometric nickel and nickel–copper spinel manganites*, Int. J. Inorg. Mater. (2000) 2[5], pp. 419-426.

24 G.C. Allen, K.R. Hallam, *Characterisation of the spinels* $M_xCo_{1-x}Fe_2O_4$ *(M = Mn, Fe or Ni) using X-ray photoelectron spectroscopy*, Appl. Surf. Sci. (1996) 93[1], pp. 25-30.

25 M. Lenglet, A. D'Huysser, J. Kasperek, J.P. Bonnelle, J. Durr, *Characterization of the oxidation states of copper and manganese in some manganites by the analysis of the XPS spectrum, X emission and X absorption thresholds*, Mat. Res. Bull. (1985) 20[7], pp. 745-757.

26 T. Hashemi, A.W. Brinkman, *X-ray photoelectron spectroscopy of nickel manganese oxide thermisters*, J. Mater. Res. (1992) 7[5], pp. 1278-1282.

27 F. Agnoli, B. Albouy, P. Tailhades, A. Rousset, *Very high coercivity of distorted spinel iron manganites. Example of mixed-valence defect oxide* $Mn_{1,7}Fe_{1,3}o_{4+\delta}$, C. R. Acad. Sci. Paris series c (1999) 2[9-10], pp. 525-530.

28 B. Kolk, A. Albers, G.R. Hearne, H. Le Roux, *Evidence of a new structural phase of manganese-iron oxide*, Hyperfine Inter. (1988) 42[1-4], pp. 1051-1054.

29 S. Guillemet-Fritsch, S. Viguie, A. Rousset, *Structure of highly divided nonstoichiometric iron manganese oxide powders* $Fe_{3-x}Mn_x\square_{3\delta/4}O_{4+\delta}$, J. Solid State Chem. (1999) 146[1], pp. 245-252.

30 S. Gubbala, H. Nathani, K. Koizol, R.D.K. Misra, *Magnetic properties of nanocrystalline Ni-Zn, Zn-Mn, and Ni-Mn ferrites synthesized by reverse micelle technique*, Physica B (2004) 348[1-4], pp. 317-328.

31 A. Kremenovic, B. Antic, V Spasojevic, M. Vucinic-Vasic, Z. Jaglicic, J. Pirnat, Z. Trontelj, *X-ray powder diffraction line broadening analysis and magnetism of interacting ferrite nanoparticles obtained from acetylacetonato complexes*, J. Phys.: Condens. Matter. (2005) 17[27], pp. 4285-4299.

32 P. Poix, *General table of metal-oxygen characteristic distances in 6 coordination*, C. R. Acad. Sci. Paris serie c (1969) 268[12], pp. 1139-1140 ; R.J. Hill, J.R. Craig, G.V. Gibbs, *Systematics of the spinel struc ture type*, Phys. Chem. Miner. (1979) 4[4], pp. 317-339 ; H.S. O'Neill, A. Navrotsky, *Simple spinels: crystallographic parameters, cation radii, lattice energies and cation distribution*, Am. Mineral. (1983) 68[1-2], pp. 181-194.

33 J.C. Bernier, P. Poix, *Oxidation states in the mixed spinel oxide* Fe_2VO_4, Ann.Chim. (1967) 2[2], pp. 81-89.

34 a) T. Yamanaka, *Crystal structures of* Ni_2SiO_4 *and* Fe_2SiO_4 *as a function of temperature and heating duration*, Phys. Chem. Miner. (1986) 13[4], pp. 227-232 ; b) T. Yagi, F. Marumo, S. Akimoto, *Crystal structures of spinel polymorphs of* Fe_2SiO_4 *and* Ni_2SiO_4, Am. Miner. (1974) 59[5-6], pp. 486-488 ; c) R.J. Hill, *X-ray powder diffraction profile refinement of synthetic hercynite*, Am. Miner. (1984) 69[9-10], pp. 937-942 ; d) I.K. Sedler, A. Feenstra, T. Peters, *An X-ray powder diffraction study of synthetic* $(Fe,Mn)_2TiO_4$ *spinel*, Eur. J. Miner. (1994) 6[6], pp. 873-885.

35 L.W. Finger, R.M. Hazen, A.M. Hofmeister, *High-pressure crystal chemistry of spinel (MgA1$_2$O$_4$) and magnetite (Fe$_3$O$_4$): comparison with silicate spinels*, Phys. Chem. Miner. (1986) 13, pp. 215-220.

36 B. Antic, A. Kermenovic., A.S. Nikolic, M. Stoiljkovic, *Cation Distribution and Size-Strain Microstructure Analysis in Ultrafine Zn-Mn Ferrites Obtained from Acetylacetonato Complexes*, J. Phys. Chem. B (2004) 108[34], pp. 12646-12651.

37 a) S. Ammar, N. Jouini, F. Fiévet, M. Richard, C. Marhic, O. Stephan, F. Villain, C. Cartier, S. Brice, P. Sainctavit, *Influence of the synthesis parameters on the cationic distribution of ZnFe$_2$O$_4$ nanoparticles obtained by forced hydrolysis in polyol medium*, J. Non-Cryst. Solid (2004) s245-246, pp. 658-662 ; b) S. Ammar, N. Jouini, F. Fiévet, P. Molinié, Z. Beji, L.S. Smiri, J.M. Grenèche, *Magnetic properties of zinc ferrite nanoparticles synthesised by hydrolysis in polyol medium,* J. Phys.: Condense. Matter (2006) 18[], pp. 9055-9069 ;

38 a) A. Frenkel, *Solving the 3D structure of metal nanoparticles*, Z. Kristallogr. (2007) 222[], pp. 605-611 ; b) Y. Sun, A.I. Frenkel, R. Isseroff, C. Shonbrun, M. Forman, K. Shin, T. Koga, H. White, L. Zhang, Y. Zhu, M.H. Rafailovich, J.C. Sokolov, *Characterization of Palladium Nanoparticles by Using X-ray Reflectivity, EXAFS, and Electron Microscopy*, Langmuir (2006) 22[2], pp. 807–816 ; c) C.-M. Lin, T.-L. Hung, Y.-H. Huang, K.-T. Wu, M.-T. Tang, C.-H. Lee, C.T. Chen, Y.Y. Chen, *Size-dependent lattice structure of palladium studied by x-ray absorption spectroscopy*, Phys. Rev. B (2007) 75[], 125426.1-125426.6.

39 a) R. Valenzuela, S. Ammar, F. Herbst, R. Ortega-Zempoalteca, *Low Field Microwave Absorption in Ni-Zn Ferrite nanoparticles in different aggregation states*, Nanosci. & Nanotechnol. Lett. (2011) 3, pp. 598-602 ; b) T. Gaudisson, M. Artus, U. Acevedo, F. Herbst, S. Nowak, R. Valenzuela, S. Ammar, *On the microstructural and magnetic properties of fine grained CoFe$_2$O$_4$ ceramics produced by combining*

polyol process and Spark Plasma Sintering, J. Magn. Magn. Mater. (2014) 370, pp. 87-95.

40 J. Wang, C. Zeng, Z. Peng, Q. Chen, *Synthesis and magnetic properties of* $Zn_{1-x}Mn_xFe_2O_4$ *nanoparticles*, Physica B (2004) 349[1-4], pp. 124-128.

41 R. Arulmurugan, B. Jeyadevan, G. Vaidyanathan, S. Sendhilnathan, *Effect of zinc substitution on Co–Zn and Mn-Zn ferrite nanoparticles prepared by co-precipitation*, J. Magn. Magn. Mater. (2005) 288, pp. 470-477.

42 a) G. Fierro, G. Ferraris, R. Dragone, M. Lo Jacono, M. Faticanti, *catalytic activity of manganese based spinels doped with copper, cobalt and iron ions*, Catal. Today (2006) 116, pp. 38-49 ; b) K. Polychronopoulou, F. Cabello Galisteo, M. López Granados, J.L.G. Fierro, T. Bakas, A.M. Efstathiou, *Novel Fe–Mn–Zn–Ti–O mixed-metal oxides for the low-temperature removal of* H_2S *from gas streams in the presence of* H_2, CO_2, *and* H_2O, J. Catal. (2005) 236[2], pp. 205-220.

43 a) L. Xue, C. Zhang, H. He, Y. Teraoka, *Catalytic decomposition of* N_2O *over* CeO_2 *promoted* Co_3O_4 *spinel catalyst,* Appl. Catal. B: Environ. (2007) 75[3-4], pp. 167-174 ; b) N. Russo, De. Fino, G. Saracco, V. Specchia, N_2O *catalytic decomposition over various spinel-type oxides,* Catal. Today (2007) 119[1-4], pp. 228-232 ; c) D. Fino, N. Russo, G. Saracco, V. Specchia, *CNG engines exhaust gas treatment via Pd-Spinel-type-oxide catalysts,* Catal. Today, (2006) 117[4], pp. 559-563 ; d) Y. Soong, V.U.S. Rao, R.J. Gormley, B. Zhong, *Temperature-programmed desorption study on manganese-iron catalysts,* Appl. Catal. (1991) 78[1], pp. 97-108.

44 a) S. Colussi, A. Gayen, J. Llorca, C. de Leitenburg, G. Dolcetti, A. Trovarelli, *Catalytic Performance of Solution Combustion Synthesized Alumina- and Ceria-Supported Pt and Pd Nanoparticles for the Combustion of Propane and Dimethyl Ether (DME)*, Ind. Eng. Chem. Res. (2012) 51[22], pp 7510–7517 ; b) A. Ishikawa, E. Iglesia, *Dimethyl ether combustion catalyzed by supported Pd, Rh, and Pt clusters: Site requirements and reaction pathways*, J. Catal. (2007) 252[1], pp. 49-56

; c) A. Ishikawa, M. Neurock, E. Iglesia, *Structural Requirements and Reaction Pathways in Dimethyl Ether Combustion Catalyzed by Supported Pt Clusters*, J. Am. Chem. Soc. (2007) 129[43], pp 13201–13212.

45 Q. Yu, L. Yu, Y. Wang, Q. Zhang, M. Sun, Y. Huang, Y. Lu, Z. Ge, *Effect of Preparation Methods on Activation of Catalysts* $BaNi_{0.2}Mn_{0.8}Al_{11}O_{19-\delta}$ *for Dimethyl Ether Combustion*, Chinese J. Chem. Eng. (2008) 16[3], pp. 389-393.

46 a) M. Sun, L. Yu, F. Ye, G. Diao, Q. Yu, Z. Hao, Y. Zheng, L. Yuan, *Transition metal doped cryptomelane-type manganese oxide for low-temperature catalytic combustion of dimethyl ether*, Chem. Eng. J. (2013) 220, pp. 320-327 ; b) M. Sun, B. Lan, T. Lin, G. Cheng, F. Ye, L. Yu, X. Cheng, X. Zheng, *Show Affiliations Controlled synthesis of nanostructured manganese oxide: crystalline evolution and catalytic activities*, Cryst. Eng. Comm. (2013) 15, pp. 7010-7018 ; c) L. Yu, G. Diao, F. Ye, M. Sun, J. Zhou, Y. Li, Y. Liu, *Promoting Effect of Ce in Ce/OMS-2 Catalyst for Catalytic Combustion of Dimethyl Ether*, Catal. Lett. (2011) 141[1], pp 111-119.

47 a) M. Florea, M. Alifanti, V.I. Parvulescu, D. Mihaila-Tarabasanu, L. Diamandescu, M. Feder, C. Negrila, L. Frunza, *Total oxidation of toluene on ferrite-type catalysts*, Catal. Today (2009) 141[3-4], pp. 361-366 ; b) M.V. Bukhtiyarova, A.S. Ivanova, E.M. Slavinskaya, L.M. Plyasova, V.A. Rogov, V.V. Kaichev, Catalytic combustion of methane on ferrites, Studies Surf. Sci. Catal. (2010) 175, pp. 355-359.

48 Z.Y. Tian, P. Mountapmbeme Kouotou, A. El Kasmi, P. Hervé Tchoua Ngamou, K. Kohse-Höinghaus, H. Vieker, A. Beyer, A. Gölzhäuser, *Low-temperature deep oxidation of olefins and DME over cobalt ferrite*, Proceedings of the Combustion Institute (2015) 35[2], pp. 2207-2214.

49 a) R. Ghahremanzadeh, Z. Rashid, A.H. Zarnani, H. Naeimi, *Synthesis of novel spirooxindoles in water by using* $MnFe_2O_4$ *nanoparticles as an efficient magnetically recoverable and reusable catalyst*, Appl. Catal. A: General (2013) 467, pp. 270-278 ; b) J. Chen, W. Wen, L. Kong, S. Tian, F. Ding, Y. Xiong, *Magnetically Separable*

and Durable $MnFe_2O_4$ for Efficient Catalytic Ozonation of Organic Pollutants, Ind. Eng. Chem. Res. (2014) 53[15], pp. 6297-6306 ; c) A. Manikandan, M. Durka, S. Arul An, *A Novel Synthesis, Structural, Morphological and Opto-magnetic Characterizations of Magnetically Separable Spinel $Co_xMn_{1-x}Fe_2O_4$ ($0 \leqslant x \leqslant 1$) Nano-catalysts*, J. Supercond. Novel Magn. (2014) 27[12], pp 2841-2857.

50 G.G. Xia, Y.G. Yin, W.S. Willis, J.Y. Wang, S.L. Suib, *Efficient stable catalysts for low temperature carbon monoxide oxidation*, J. Catal. (1999) 185[1], pp. 91-105.

51 N. Russo, D. Fino, G. Saracco, V. Specchia, N_2O catalytic decomposition over various spinel-type oxides, *Air Pollution Abatement Catal. Symposium* (2007) 119[1-4], pp. 228-232.

Polyol synthesis of non-stoichiometric Mn-Zn ferrite nanocrystals: structural /microstructural characterization and catalytic application.